Using Mechanically-Induced Long-Period Fiber Gratings for OAM Modes Generation Based on Anti-Resonant Mechanisms in Ring-Core Fibers

Jianheng Qiu, Fufei Pang, *Member, IEEE*, Liang Zhang, Heming Wei, *Member, IEEE*, Yana Shang, Wei Chen, Sujuan Huang, and Tingyun Wang

***Abstract*—A flexible first-order OAM modes generation in ring-core fibers (RCFs) based on a mechanically-induced long-period fiber grating (MLPFG) is proposed. By directly fusion splicing a standard single-mode fiber (SMF) and RCFs, the anti-resonant reflection guidance mechanism (ARRGM) is introduced in the RCF, leading to the guided-core modes, so-called anti-resonant modes (AR modes), which have a Gaussian field distribution and are confined in low-refractive index central core of RCFs. A mechanical long-period fiber grating is used to couple the AR modes into the OAM modes propagated in the high-index ring core of the RCF. Results show that the generated OAM modes are the combination of two orthogonal linearly polarized (LP) modes with $\pm\pi/2$ phase shift in the ring core. The mode conversion efficiency of OAM_{+1} and OAM_{-1} can reach 95% and 94%, respectively, indicating promising applications in sensing and communication of the RCFs.**

***Index Terms*—Anti-resonant reflection guidance, long-period fiber gratings, orbital angular momentum, ring-core fiber.**

I. Introduction

Structured lights have complex distribution of polarization, phase or intensity. In particular, the orbital angular momentum (OAM) gives the beam a special spatial structure, which is another degree of freedom besides frequency and polarization. Structured light has found wide applications in the fields of optical imaging, optical communication, and atomic manipulation [1]. The OAM with a helical phase front, in which the central intensity of the vortex beam is zero, shows the field intensity distribution of a doughnut-like shape. Furthermore, following the propagation direction of the optical axis, the wave vector appears as a spiral, and the topological charge number (L) is used to describe its order. Theoretically, the topological charge number L can be infinite, which is beneficial for OAM-division multiplexing technique in the communication field. All-fiber generation of vortex beam offers the advantages of stability and flexibility [2], which can facilitate the system integration and the adaptability of the communication link [3]. The choice of OAM fiber and the corresponding all-fiber OAM mode generation scheme are particularly crucial.

The ring-core fibers (RCFs) [4], which have a ring-shaped refractive index profile to adapt to the OAM mode field, can perfectly carry the OAM modes. The RCFs with higher refractive index difference can minimize the intermodal coupling among the OAM modes. How to efficiently generate OAM modes in RCFs has always been a hot research topic. On the one hand, relying on special splicing technology, the offset splicing method has accomplished the generation of the second-order OAM mode [5], however, the stability is poor. Meanwhile, generation of the OAM mode has no wavelength selectivity. On the other hand, relying on high-energy laser technology, although the method of etching gratings on the fiber has good stability [6], it lacks flexibility and the fiber cannot be reused. Mechanically induced long-period fiber gratings (MLPFGs) can not only generate modes in fibers with better wavelength selectivity, but also have flexible control of the depth attenuation and bandwidth of notch bands without damage to the fibers [7]. It has application in many fields, such as fiber optic sensors [8], filters [9], mode converters [10], *etc*.

Anti-resonant reflection guidance mechanism (ARRGM) exists in the wave-guide structure that has a high refractive index structure surrounding the low refractive index core. This waveguide structure is defined as anti-resonant reflective optical wave-guide (ARROW). Many fibers have been verified to utilize ARRGM, such as photonic crystal fiber, hollow-core fibers, negative curvature fiber, and Kagome fibers [11]. In the ARROW, the light beam is continuously reflected and refracted at the high-low refractive index interface. Multiple beams interfere in the low refractive index core and the light is finally confined and propagated within the fiber. When the incident light meets the resonant condition, it leaks out of the cladding, which is defined as the leakage mode. On the contrary, the light is defined as the anti-resonant mode (AR mode). The fibers based on ARRGM have been employed for various sensing applications

Manuscript received December 29, 2021; revised February 26, 2022; accepted March 7, 2022. Date of publication March 15, 2022; date of current version March 31, 2022. This work was supported in part by the National Natural Science Foundation of China under Grants 61975108, 61875118, 61905138, and 62005153, in part by the Science and Technology Commission of Shanghai Municipality under Grants 20ZR1420300 and 20ZR1420800, and in part by 111 Project under Grant D20031. *(Corresponding author: Fufei Pang.)*

The authors are with the Key Laboratory of Specialty Fiber Optics and Optical Access Networks, Joint International Research Laboratory of Specialty Fiber Optics and Advanced Communication, Shanghai Institute for Advanced Communication and Data Science, Shanghai University, Shanghai 200444, China (e-mail: 765894282@shu.edu.cn; ffpang@shu.edu.cn; liangzhang@shu.edu.cn; hmwei@shu.edu.cn; ynshang@shu.edu.cn; chenweisd@shu.edu.cn; sjhuang@shu.edu.cn; tywang@shu.edu.cn).

Digital Object Identifier 10.1109/JPHOT.2022.3159112

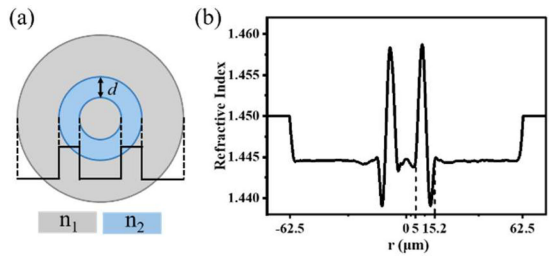

Fig. 1. (a) Schematic diagram of the one-layer-ring ARROW model (n2 > n1). (b) The measured refractive index distribution of the RCF.

[12]. Furthermore, AR modes can be transmitted stably in optical fibers, which has the potential to generate higher-order modes.

In this paper, the ARRGM in RCFs is analyzed and a MLPFG is used to generate the first-order OAM modes. By directly fusion splicing the RCF and a standard single-mode fiber (SMF), it is found that the output spot of the RCF presents a Gaussian field distribution. The transmission spectrum of the RCF indicates that the resonant wavelength is consistent with the theoretical results of the ARRGM. The finite element method is used to numerically simulate the modes in the RCF, in which the effective mode refractive index (n_{eff}) of the AR modes is calculated. The MLPFG is used to couple the AR modes in the low refractive index central core to the OAM modes in the high refractive index ring core at the wavelength of 1525 nm accurately. The mode conversion efficiency of OAM_{+1} and OAM_{-1} can reach 95% and 94%, respectively. It provides a new solution for the OAM modes generation in the RCFs, which is benefit to construct all-fiber OAM system.

II. Theory

A. AR Modes in the RCF

Concerning to the ARROW structure of fibers, they are mainly classified as: (1) Concentric ring fiber composed of high-index layers; (2) Micro-structured optical fiber with high-index cylindrical inclusions [13]. The hollow-core fiber belongs to the former, typically. It has a low-index air cladding structure with higher transmission loss. Increasing the number of high-low refractive index layers can decrease the propagation loss of the ARROW [14]. A one-layer-ring model of the ARROW as shown in Fig. 1(a). Light beams undergo multiple anti-resonant reflections between the high and low refractive index layers, which provides additional restrictions on the central core region. Each layer can be considered as a radial F-P cavity [13]. The narrow-band resonant wavelength of the F-P resonator corresponds to the leakage modes in the ARROW, while the wide anti-resonant wavelength corresponds to the AR mode in the low refractive index central core.

Fig. 1(b) shows the refractive index profile of the used RCF, which is classified as the one-layer-ring ARROW model. The thickness of the high refractive index ring core, $d = 5.4$ μm, the diameter of the low refractive index central core is 10.8 μm, and $n_1 = 1.4440$, $n_2 = 1.4579$. The ray theory is used to illustrate the ARRGM in the one-layer-ring ARROW structure as shown in Fig. 2(a) [15]. Under the small-scale model, the constant

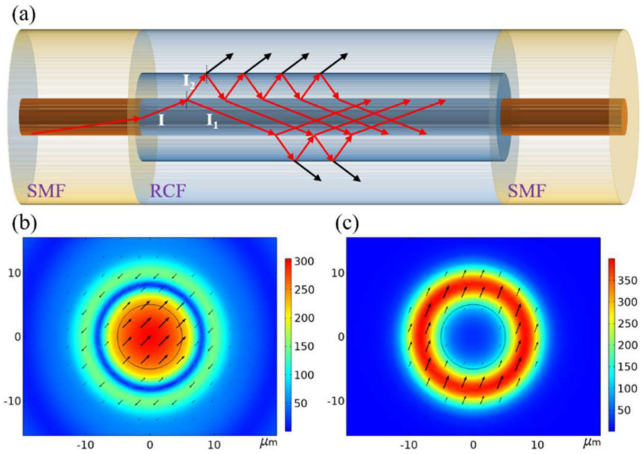

Fig. 2. (a) The schematic diagram of multi-beam optical path in the RCF, the red arrows represent anti-resonant wavelength. (b) Modes field distribution of the AR mode, and (c) the HE_{11} mode by the simulation.

waveguide frequency of the RCF ($V = 8.8$ here) is closed to the condition of ray theory approximation basically ($V \gg 1$) [16]. Although this treatment with the ray theory approximation may cause some errors in the accurate numerical simulation, the working principle can be demonstrated clearly. When the SMF and the RCF are directly fused, the incident light from the SMF undergoes the first reflection (I_1) and refraction (I_2) at the high-low refractive index interface of the RCF. Further, I_2 is reflected in the high refractive index ring core, and refracted again into the low refractive index central core to interfere with I_1. The guided-core modes propagate at glancing angles in the low index core.

Based on the double-beam interference model, the resonant conditions can be derived from the optical path difference [15]:

$$\lambda_m = \frac{2d}{m}\sqrt{n_2^2 - n_1^2} \tag{1}$$

where m is the resonant order.

When the working wavelengths satisfy the resonant condition, the beams destructively interfere in the central core, while a standing wave is formed in the high-index layer and propagates forward. On the contrary, the beams are confined in the low-index central core and the AR mode is formed.

B. Numerical Simulation of Modes in the RCF

According to the parameters of the RCF, based on the optical waveguide theory, the finite element method is used to calculate the n_{eff} of the modes in the RCF. And the field distribution of an AR mode and a HE_{11} mode are shown in Fig. 2(b) and (c). It can be found that the energy is mainly concentrated in the low refractive index central core, which is different from the HE_{11} mode in the ring core. The AR mode has $n_{eff} = 1.4429$, which is lower than the refractive index of the central core. Furthermore, the RCF supports vector modes TM_{01}, HE_{21}, and TE_{01} required to generate first-order OAM modes. Fig. 3(a) compares the n_{eff} of these modes in the RCF as a function of the wavelength. At the wavelength of 1550 nm, the n_{eff} differences between HE_{21} and TE_{01}, HE_{21} and TM_{01} are all

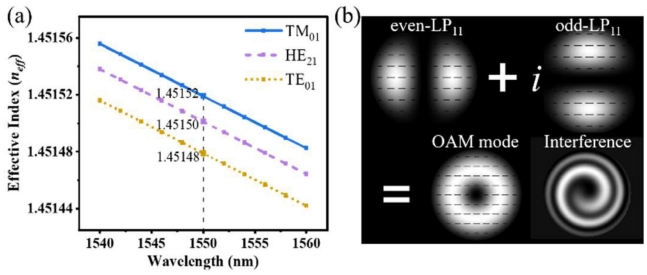

Fig. 3. (a) Calculated n_{eff} of vector modes versus wavelength. (b) A simulation of OAM mode generation. The black line segments represent the polarization state of the modes.

less than 10^{-4}. In other words, when multiple vector modes propagate in the fiber simultaneously, the mode degeneration occurs among the vector modes. Therefore, the final output of the RCF is a linear polarization (LP) mode [17]. Finally, the linearly polarized OAM modes in the RCF can be generated by combining degenerated $\mathrm{LP}_{11}^{\mathrm{odd}}$ and $\mathrm{LP}_{11}^{\mathrm{even}}$ modes with a $\pm\pi/2$ phase shift [18]. Fig. 3(b) illustrates the principle of OAM mode generation by a simulation, and this process can be described by the formula, $\mathrm{LP}_{11}^{\mathrm{even}} \pm \mathrm{iLP}_{11}^{\mathrm{odd}} = \mathrm{OAM}_{\pm 1}$.

C. The Method of Modes Generation

In order to generate OAM modes in the RCF based on the AR mode, ultra-long period fiber grating (ULPFG) is utilized. The ULPFG is essentially one kind of diffraction gratings. With the phase matching condition of diffraction orders [19],

$$\lambda_{res} = \left(n_{HE_{21}} - n_{AR}\right) \frac{\Lambda}{N} \tag{2}$$

where Λ is the grating period, N is the diffraction order, $n_{HE_{21}}$ and $n_{AR}$are the n_{eff} of the HE_{21} mode and the AR mode, respectively. If a regular long period fiber grating is considered, the value of N is 1. In this work, in order to make the resonant wavelength λ_{res} reach the telecommunication wavelength 1550 nm, the Λ is set as around 180 μm. To enhance the reusability of the fiber, the MLPFG method is adopted instead of the etching grating method. However, the grating period is too small, which makes it difficult to produce the MLPFG using commercial 3D printing technology with 0.1 mm precision. Therefore, the ULPFG principle is considered, and the grating period is appropriately enlarged to increase the number of diffraction orders and ensure that its resonant wavelength is around 1550 nm.

The grating refractive index distribution function is the essential part of the fiber grating theory [20],

$$\Delta n\ (r, \Phi, z) = \Delta n_0 + \Delta n \bullet \sigma\,(z)\, S\,(z)\, P\,(r, \Phi, z) \tag{3}$$

where $S(z)$ is axial refractive index change of the fiber, $\sigma(z)$ is apodization function, $P(r, \Phi, z)$ is cross-sectional refractive index distribution of fiber, Δn_0 represents the average refractive index change of the grating. Δn represents the magnitude of the refractive index change of the grating.

Theoretically, the axial refractive index change of the fiber presents a periodic rectangular distribution $s\ (z) = \sum_{k=0}^{N} \prod(\frac{z-k\Lambda}{a})$. With the Fourier expansion, the axial refractive index distribution can be expanded as [20]

$$S\ (z) = \sum_{m=-\infty}^{+\infty} \frac{\sin(m\pi)\, a}{m\pi\Lambda}\, e^{jm\frac{2\pi}{\Lambda}}$$

$$\approx \frac{a}{\Lambda} + \sum_{N\,=\,1}^{k} C_N \cos\left(N\frac{2\pi}{\Lambda}z\right) \tag{4}$$

where a is the pulse width of the rectangular function, $C_N = [2/(N\pi)]\ \sin(N\pi a/\Lambda)$ is the coefficients of $S(z)$. For conventional gratings with a period of several hundred microns, the high-order C_N in the $S(z)$ is too small to have much influence on the depth of the resonant dip in the transmission spectrum. However, with the increase of Λ, the high-order C_N cannot be ignored. Therefore, it is found that the transmission spectrum of ULPFG is acted by sub-gratings with different spatial frequencies $(2N\pi/\Lambda)$ [20]. And the refractive index distribution $\Delta n(r, \Phi, z)$ is closely related to C_N, the mode coupling coefficient of the *N-th* diffraction order is finally promoted. The ratio, C_N/C_1, can be used to reflect the influence of the *N-th* sub-gratings on the spectrum.

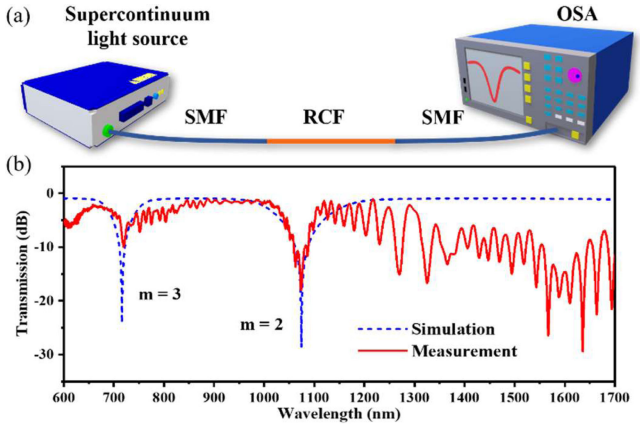

Fig. 4. (a) Experimental setup, (b) simulation and measurement result of the RCF transmission spectrum.

III. Experimental Setup and Results

In order to verify the spectral characteristics of the ARRGM in the RCF, the transmission spectrum of SMF-RCF-SMF structure is measured. Experimental setup is shown in Fig. 4(a). The supercontinuum source (YSL Photonics, SC-5) is launched to a 1 cm RCF through a SMF by directly fusion splicing, and the RCF is then connected to an optical spectrum analyzer (OSA) with another SMF in the same way.

The measurement result of the RCF transmission spectrum is shown in Fig. 4(b). There are two main dips at the wavelengths of 720 nm and 1074 nm. According to the one-layer-ring ARROW structure [21], the transmission spectrum of the RCF is also simulated with the parameters in Fig. 1(b), as shown in Fig. 4(b). The wavelengths of the resonant dips in the simulation result are in good agreement with the measurement result. And the wavelengths at 715 nm and at 1075 nm of the two dips correspond to

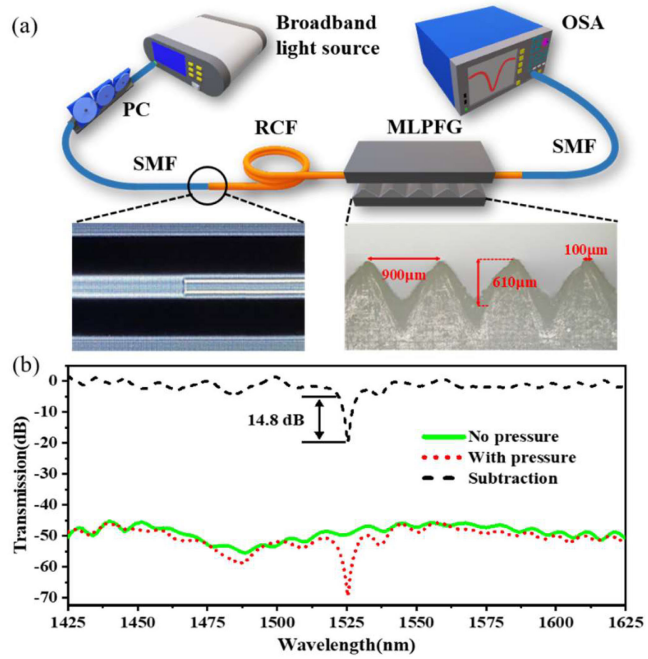

Fig. 5. (a) Experimental setup for generation of higher-order modes using the MLPFG. Illustration: (left inset) Fusion splicing between the RCF and the SMF, (right inset) structure and relevant parameters of the MLPFG under the microscope. (b) The transmission spectrum compares the two states with (red line) and without (green line) pressure.

the resonant orders of $m = 3$ and $m = 2$, respectively. For the experiment, on the anti-resonant waveband (longer than 1100 nm), the transmission spectrum presents multiple fringes which result from the modal interference effect. The splicing point between the input SMF with the RCF may cause higher-modes excitation which can interfere at the second splicing point. It is not considered in the simulation.

In order to couple the AR mode in the low-index central core into the HE_{21} mode in the high-index ring core, the MLPFG is used to exert pressure on one side of the RCF. The elasto-optical effect occurs under the lateral pressure. The refractive index of the fiber is changed periodically along the axial direction. When the working wavelengths satisfy the phase matching condition, the energy can be transferred from the AR modes in the central core to the modes in the ring core. In addition, the effect of stress-induced birefringence increases the difference of n_{eff} between the orthogonal LP modes. The two LP modes with different phase velocity can achieve a $\pm\pi/2$ phase shift at the end of RCF [22], [23].

Using 3D printing technology, the resin material is made into a zigzag-shaped MLPFG. The number of the grating periods is set as 50. The structure and size of the MLPFG is measured by a microscope, as shown in the right inset of Fig. 5(a), the width of the serration tip, $a = 100$ μm, and average period of the MLPFG is 900 μm. Due to the limitation of experimental equipment, the grating period should not be set too large, because a greater period of the grating leads to fewer number of periods and the coupling efficiency is reduced subsequently [24]. According to Eq. (2), when $N = 5$, the resonant wavelength is around 1548

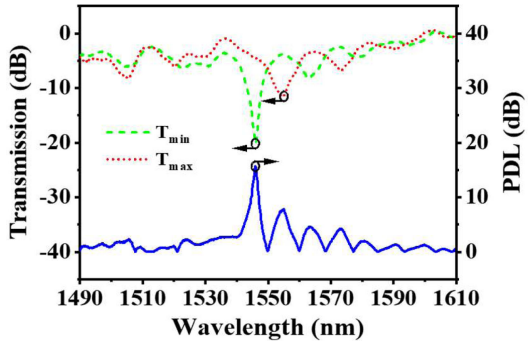

Fig. 6. Transmission (left axis) and PDL (right axis) spectrum of the MLPFG.

nm. And $C_5/C_1 = 58\%$ according to C_N in Eq. (4). In addition, enough depth of sawtooth should be ensured to enhance the fiber deformation and improve its coupling efficiency.

Fig. 5(a) shows experimental setups for generation of higher-order modes using the MLPFG. A broadband light source (Super luminescent diode, OS8145) is used as the input. The SMF and the RCF are directly fused, and the core diameter of the SMF is 9 μm, which is slightly smaller than the central core of the RCF (10.8 μm). Fusion spliced fibers are shown in the left inset of Fig. 5(a). At the output end of the RCF, it is difficult for energy from the ring core to be coupled into the output SMF. Therefore, the wavelength where the higher-order modes appear can be discerned according to the resonant dips in the transmission spectrum.

The transmission spectrum of the SMF-RCF-SMF structure was analyzed using the OSA, in which the length of RCF is 40 cm. Increasing the length of the RCF can narrow the free spectral range of the modal interference in Fig. 4(b), and the continuous leakage of interfering modes resulting in the weakening of interference intensity. Therefore, the interference fringes gradually weaken, the spectrum in working waveband is flat and conducive to OAM modes generation. By using the 900 μm-MLPFG to exert external pressure on the RCF, it can be found that higher-order modes are stably generated at the wavelength of 1525 nm, and the depth of the resonant dip can reach 14.8 dB. Considering the accuracy of the 3D printing technology and the offset of fiber placement position, the experimental results have a 23 nm deviation from the theoretical calculation.

Fig. 6 shows the polarization dependent loss (PDL) characteristic of the MLPFG transmission spectrum. An additional fiber polarizer converts the input light into linearly polarized light. Maximum and minimum transmission spectrum (T_{max} and T_{min}) were recorded using the OSA by adjusting the PC. The PDL spectrum is calculated from the absolute value of the difference between T_{max} and T_{min}. The MLPFG exerts pressure on one side of the RCF, which results in a non-uniform distribution of force across the fiber cross-section. Therefore, the transmission spectrum of the MLPFG has a certain polarization dependence. A birefringence compensation method can improve the PDL characteristics of the MLPFG [25].

In order to further analyze the characteristics of higher-order modes generated by the MLPFG, the experimental setups are

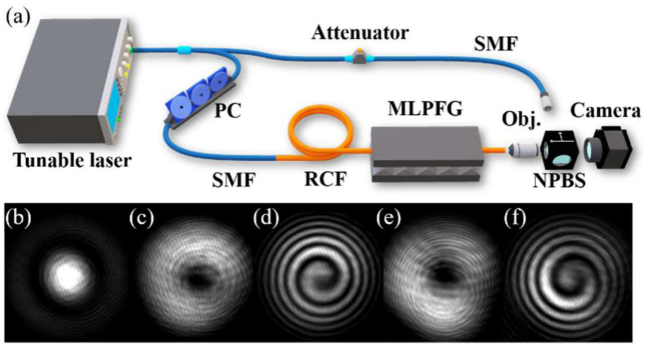

Fig. 7. (a) Experimental setup for OAM modes generation and detection. PC: polarization controller, NPBS: non-polarization beam splitter, (b) field distribution of the AR mode. Mode field distribution and interference pattern of the OAM modes with $L = +1$ (c) and (d), $L = -1$ (e) and (f).

shown in Fig. 7(a). The working wavelength of the tunable laser (Keysight 81600B) is set at 1525 nm, and the output field of the RCF is captured by an infrared camera. Without any pressure on the MLPFG, the output field of the RCF presents a Gaussian field distribution, as shown in Fig. 7(b). It indicates that the AR mode transmitted in the low refractive index central core of the RCF. Therefore, the AR mode has no notch band in the transmission spectrum (the green line in Fig. 5(b)). Exerting pressure on the MLPFG, a standard mode with ring-shaped field distribution is captured, as shown in Fig. 7(c) and (e). The interference patterns indicate that the OAM_{+1} and OAM_{-1} modes are generated, as shown in Fig. 7(d) and (f). Different pressures can induce different phase shift between the orthogonal LP_{11}^{odd} and LP_{11}^{even} modes, which is used for selective generation of OAM_{+1} and OAM_{-1} modes [23], [24].

An additional linear polarizer is placed in front of the camera to detect the polarization state of the generated OAM modes. Changing the angle of the fast axis of the linear polarizer, the output mode fields of OAM_{+1} and OAM_{-1} are recorded with their interference patterns, as shown in Fig. 8(a) and (b). It can be found that both OAM_{+1} and OAM_{-1} have the same linear polarization.

As changing the direction of the polarizer, the field intensity of two OAM modes alternate between bright and dark, and the interference patterns show a spiral shape. It can be proved that the polarization state of the first-order OAM mode is linear polarization. It means that the principle of OAM modes generation is a combination of two orthogonal LP_{11} modes with a $\pm\pi/2$ phase difference. By calculating the resonant wavelength of TM_{01}, TE_{01}, and HE_{21} modes, there is only a 2 nm difference. Therefore, these three modes cannot be distinguished independently in the RCF, the degenerated LP modes are generated. Finally, the OAM modes can be generated by adjusting the pressure on the MLPFG and the PC.

The scalar intensity analysis method is used to calculate the purity of OAM modes [26]. The OAM_{+1} and OAM_{-1} modes from the first column of Fig. 8(a) and (b) are calculated by the method, which can reach 98.64% and 96.71%, respectively. The OAM_{+1} and OAM_{-1} mode fields are collected every 10 minutes for an hour and their purity parameters are calculated, as shown

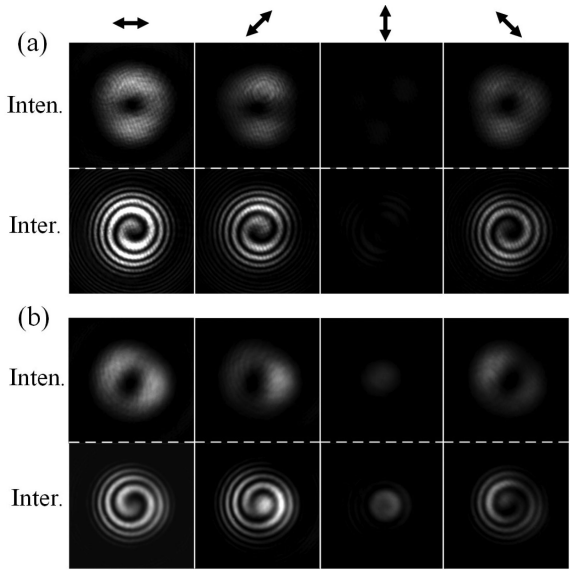

Fig. 8. The intensity and interference patterns of OAM_{+1} and OAM_{-1} modes in (a) and (b), respectively. Double-sided arrows denote the polarizer directions, increasing the degree by 45° per column. Inten., intensity, Inter., interference.

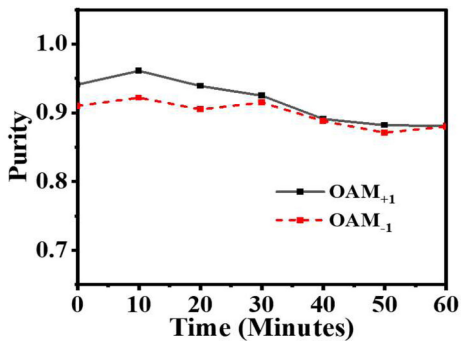

Fig. 9. Stability of OAM modes purity with time.

in Fig. 9. The purity parameter has a slight downward trend with time, which may be caused by the loosening of the pressure device.

Before and after applying the MLPFG, the output power of RCF is tested for the AR mode and the excited OAM modes by using a power meter, respectively, at the resonant wavelength of the MLPFG. The excitation efficiency of the MLPFG is calculated as approximate 97% for both OAM_{+1} and OAM_{-1} modes. Therefore, based on the purity of the OAM modes, the mode conversion efficiency of OAM_{+1} and OAM_{-1} can be derived as 95% and 94%, respectively.

IV. Conclusion

The ARRGM in the RCF used for $OAM_{\pm1}$ mode generation is proposed and demonstrated. By directly fusion splicing of the SMF and the RCF, the AR mode with a Gaussian field distribution is generated, which propagates in the low refractive index central core. The MLPFG produced by 3D printing technology excited the AR modes into the OAM_{+1} and OAM_{-1} modes, in which the resonant wavelength is controllable. And

the generated OAM modes are a combination of orthogonal LP_{11} modes with a $\pm\pi/2$ phase shift. Moreover, the OAM beams can be generated using a flexible MLPFG and the method of directly fusion splicing, exhibiting the characteristics of simplicity, low-cost, and controllability. As a special mode in RCF, the AR mode is proposed for high-efficiency generation of the first-order OAM modes, which provides a significant guidance for the generation of higher-order OAM modes in RCFs. The proposed all-fiber OAM modes generation system has potential applications, such as sensing, detection, optical manipulation, and imaging.

REFERENCES

[1] D. Andrews, *Structured Light and Its Applications*. U.K.: Academic, 2008.

[2] Y. Zhao, T. Wang, C. Mou, Z. Yan, Y. Liu, and T. Wang, "All-fiber vortex laser generated with few-mode long-period gratings," *IEEE Photon. Technol. Lett.*, vol. 30, no. 8, pp. 752–755, Apr. 2018.

[3] N. Bozinovic *et al.*, "Terabit-scale orbital angular momentum mode division multiplexing in fibers," *Science*, vol. 340, no. 6140, pp. 1545–1548, Jun. 2013.

[4] C. Brunet, B. Ung, L. Wang, Y. Messaddeq, S. LaRochelle, and L. A. Rusch, "Design of a family of ring-core fibers for OAM transmission studies," *Opt. Exp.*, vol. 23, no. 8, pp. 10553–10563, Apr. 2015.

[5] W. Song *et al.*, "Excitation of high-order optical vortex modes by tilting tapered and lensed single mode fiber," *Chin. J. Lasers*, vol. 46, no. 9, Sep. 2019, Art. no. 0906001.

[6] Y. Han *et al.*, "Controllable all-fiber generation/conversion of circularly polarized orbital angular momentum beams using long period fiber gratings," *Nanophotonics*, vol. 7, no. 1, pp. 287–293, Jan. 2018.

[7] I. Torres-Gómez, D. E. Ceballos-Herrera, and K. M. Salas-Alcantara, "Mechanically-induced long-period fiber gratings using laminated plates," *Sensors*, vol. 20, no. 9, May 2020, Art. no. 2582.

[8] Y. Tsutsumi, M. Ohashi, and Y. Miyoshi, "Temperature sensing using an optical time domain reflectometer and mechanical long-period fiber gratings fabricated from a heat-shrinkable tube," *IEICE Commun. Exp.*, vol. 6, no. 2, pp. 103–108, Aug. 2017.

[9] U. P. Sunita and M. Vivekanand, "Tunable optical filter based on mechanically induced cascaded long period optical fiber grating," *J. Photon.*, vol. 2013, May 2013, Art. no. 415059.

[10] Y. C. Jiang, G. B. Ren, Y. D. Lian, B. Zhu, W. Jin, and S. Jian, "Tunable orbital angular momentum generation in optical fibers," *Opt. Lett.*, vol. 41, no. 15, pp. 3535–3538, Aug. 2016.

[11] N. Cai, L. Xia, and Y. Wu, "Multiplexing of anti-resonant reflecting optical waveguides for temperature sensing based on quartz capillary," *Opt. Exp.*, vol. 26, no. 25, pp. 33501–33509, Dec. 2018.

[12] W. J. Ni *et al.*, "Recent advancement of anti-resonant hollow-core fibers for sensing applications," *Photonics*, vol. 8, no. 4, pp. 1–13, Apr. 2021, Art. no. 128, doi: 10.3390/photonics8040128.

[13] N. Litchinitser *et al.*, "Resonances in microstructured optical waveguides," *Opt. Exp.*, vol. 11, no. 10, pp. 1243–1251, May 2003.

[14] N. Litchinitser, A. Abeeluck, C. Headley, and B. J. Eggleton, "Antiresonant reflecting photonic crystal optical waveguides," *Opt. Lett.*, vol. 27, no. 18, pp. 1592–1594, Sep. 2002.

[15] X. Zhang *et al.*, "Transition of Fabry-Perot and antiresonant mechanisms via a SMF-capillary-SMF structure," *Opt. Lett.*, vol. 43, no. 10, pp. 2268–2271, May. 2018.

[16] A. W. Snyder and J. D. Love, *Optical Waveguide Theory*. London, ON, Canada: Chapman & Hall, 1983.

[17] S. Ramachandran and P. Kristensen, "Optical vortices in fiber," *Nanophotonics*, vol. 2, no. 5-6, pp. 455–474, Jan. 2013.

[18] Y. Jiang *et al.*, "Tunable orbital angular momentum generation based on two orthogonal LP modes in optical fibers," *IEEE Photon. Technol. Lett.*, vol. 29, no. 11, pp. 901–904, Jan. 2017.

[19] X. Shu, L. Zhang, and I. Bennion, "Fabrication and characterisation of ultra-long-period fibre gratings," *Opt. Commun.*, vol. 203, no. 3-6, pp. 277–281, Mar. 2002.

[20] T. Zhu, "Study on special long-period fiber gratings," Ph.D. dissertation, Dept. Opto-Electron. Eng., Chongqing Univ., Chongqing, China, 2008.

[21] W. Sun *et al.*, "Comparative study on transmission mechanisms in a SMF-capillary-SMF structure," *J. Lightw. Technol.*, vol. 38, no. 15, pp. 4075–4085, Aug. 2020.

[22] N. Bozinovic, S. Golowich, P. Kristensen, and S. Ramachandran, "Control of orbital angular momentum of light with optical fibers," *Opt. Lett.*, vol. 37, no. 13, pp. 2451–2453, Jul. 2012.

[23] Y. Zhang *et al.*, "Generation of the first-order OAM modes in ring fibers by exerting pressure technology," *IEEE Photon. J.*, vol. 9, no. 2, Apr. 2017, Art. no. 7101609.

[24] S. Li, Q. Mo, X. Hu, C. Du, and J. Wang, "Controllable all-fiber orbital angular momentum mode converter," *Opt. Lett.*, vol. 40, no. 18, pp. 4376–4379, Sep. 2015.

[25] J. Cho and K. Lee, "A birefringence compensation method for mechanically induced long-period fiber gratings," *Opt. Commun.*, vol. 213, no. 4-6, pp. 281–284, Dec. 2002.

[26] Y. Jiang *et al.*, "Linearly polarized orbital angular momentum mode purity measurement in optical fibers," *Appl. Opt.*, vol. 56, no. 7, pp. 1990–1995, Mar. 2017.